Supporting Material to

"Microtubule feedback and LET-99-dependent control of pulling forces ensure robust spindle position."

Hélène Bouvrais[1,*], Laurent Chesneau[1], Sylvain Pastezeur[1], Danielle Fairbrass[1], Marie Delattre[2], and Jacques Pécréaux[1,*]

Affiliations

[1] CNRS, Univ Rennes, IGDR – UMR 6290, F-35000 Rennes, France.

[2] Univ Lyon, ENS de Lyon, Univ Claude Bernard, Laboratory of Biology and Modelling of the Cell, Lyon University, Lyon, France

Correspondence: helene.bouvrais@univ-rennes1.fr (ORCID # 0000-0003-1128-1322); jacques.pecreaux@univ-rennes1.fr (ORCID # 0000-0001-9998-4844)

Supplemental Figures to "Microtubule feedback and LET-99-dependent control of pulling forces ensure robust spindle position."

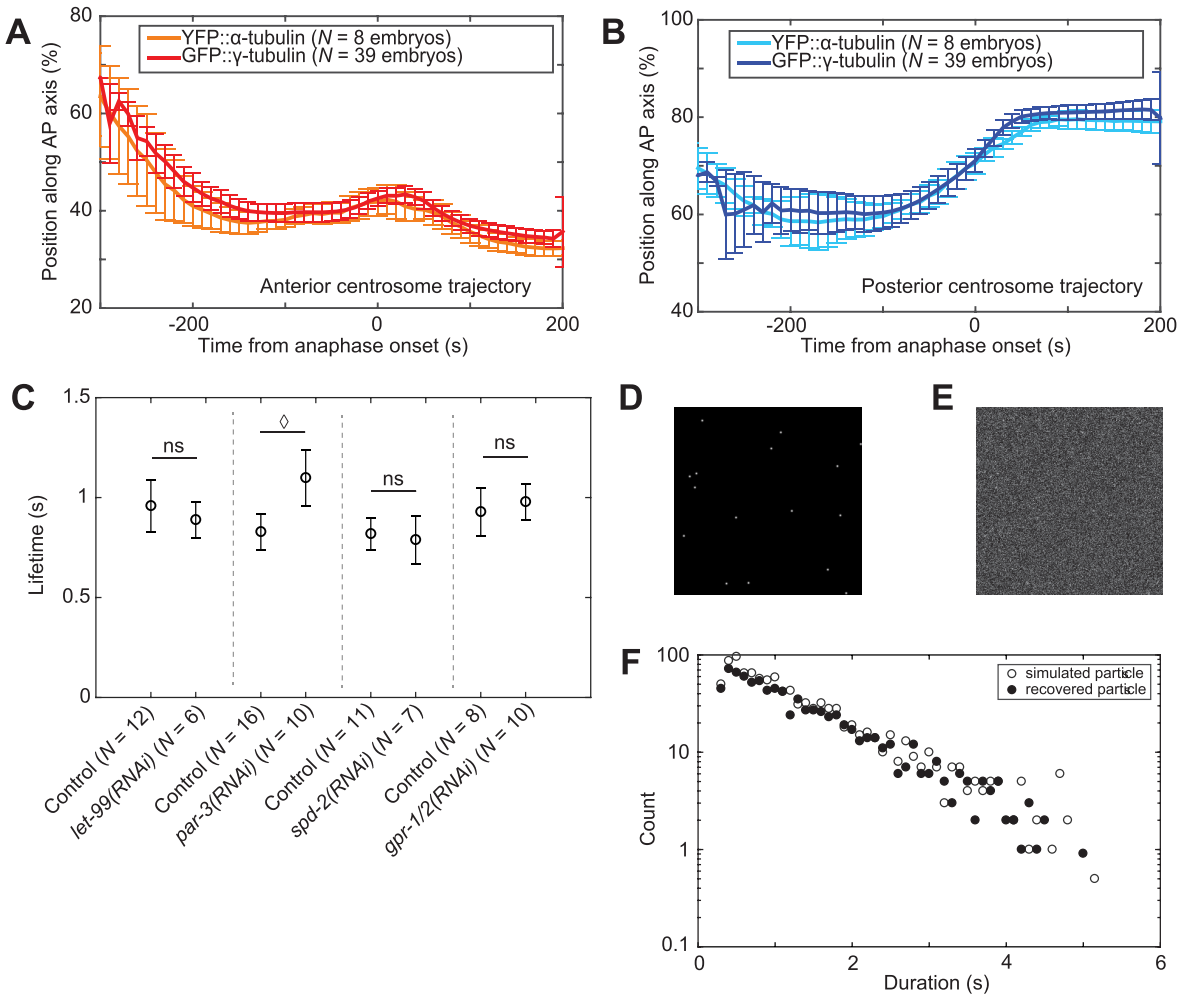

Figure S1: Validation of the strain and the analysis pipeline used to measure microtubule contact density at the cell cortex.

(**A-B**) Comparison of the (A) anterior and (B) posterior centrosome trajectories during mitosis between two *C. elegans* strains at 23°C, one with YFP::α-tubulin–labeled microtubules (orange and light-blue lines, N = 8 embryos) and the other with GFP::γ-tubulin-labeled centrosomes (red and dark-blue lines, N = 39 embryos). The positions along the anteroposterior (AP) axis are shown as a percentage of embryo length. (**C**) Residence times of microtubules at the cortex in the various *RNAi* treatment conditions used to challenge our full-expanded model (Suppl. Methods in the Supporting Material). Error bars indicate SD and diamond indicates a significant difference (Methods). (**D-E**) Fabricated images with particles of known dynamics and their analysis to validate the image-processing pipeline (Suppl. Methods). (D) We simulated particles (bright spots) that mimic the microtubule contacts at the cortex. (E) We then added noise to mimic the background observed experimentally. (**F**) Finally, we compared the histograms of particle lifetimes provided to the simulation (open circles) with those recovered through our analysis (closed symbols). The parameters used to fabricate *in silico* microtubule cortical contact dynamics images are listed in Supplemental Methods.

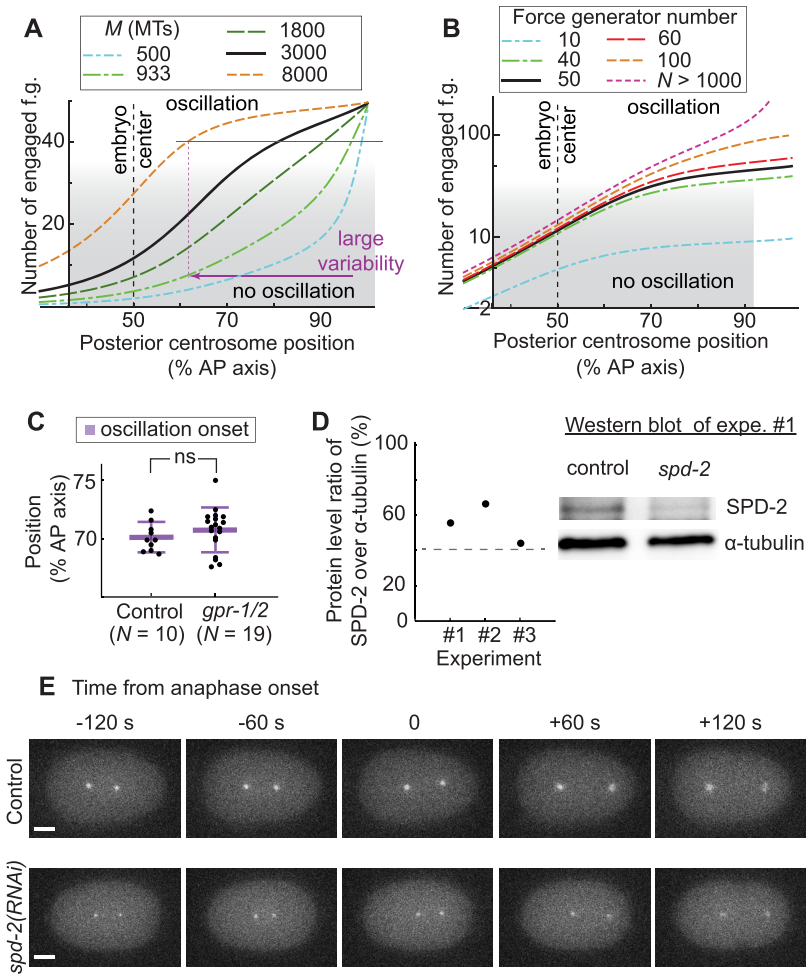

Figure S2: Microtubule number affects the oscillation onset position, while force generator quantity above a threshold does not.

(**A-B**) Modeled number of engaged force generators (f.g.) versus the posterior displacement of the centrosome along the anteroposterior (AP) axis as a percentage of the embryo length: variations (A) in total number of microtubules *M* emanating from a single centrosome and (B) in total number of force generators *N*. In both cases, control values are black; green and blue are lower values; and red and orange are higher ones. The parameters used are listed in Table S5. Grey shading indicates when the number of engaged force generators was too low to permit oscillation (below threshold). Thin purple lines give a variability scale. (**C**) Posterior centrosome position at oscillation onset upon depletion of active force generators through *gpr-1/2(RNAi)* (*N* = 19 embryos) compared to *N* = 10 control embryos, both with GFP::γ-tubulin labeling of centrosomes. Bee swarm plot reports values obtained for each embryo. Large thick horizontal bars depict the mean while error bars indicate SD. (**D**) Western blot of worm lysates treated by *spd-2(RNAi)* or control vector. Left panel depicts the ratio of SPD-2 to α-tubulin (loading control) protein levels, in triplicate, while the right panel reproduces an exemplar blot (Methods). (**E**) Stills of *C. elegans* embryos with GFP::γ-tubulin-labeled centrosomes in control condition, i.e. treatment using empty L4440 vector (top row), and upon *spd-2(RNAi)* treatment (bottom row). Anaphase onset is the reference time. Posterior tip of embryo is on the right hand side of the picture. Scale bars represent 10 μm.

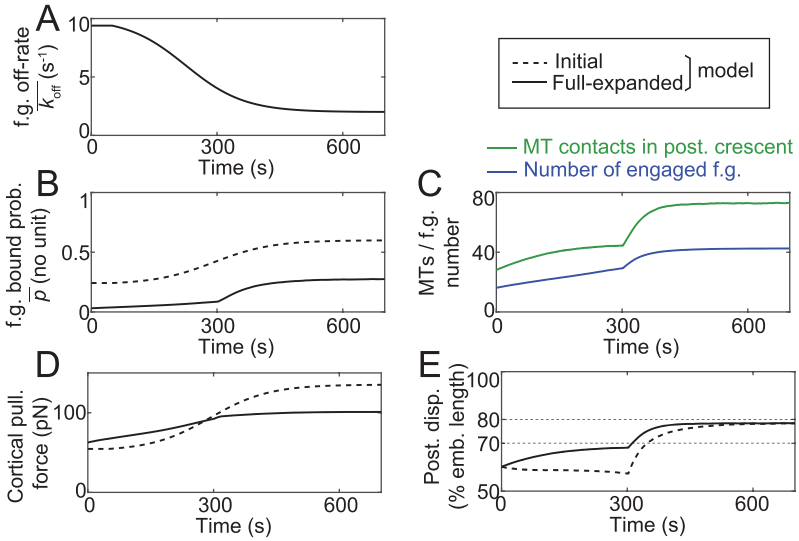

Figure S3: Simulation of the displacement of the posterior centrosome using the full-expanded model.

Typical run showing: (**A**) the force generator (f.g.) detachment rate (inverse of processivity), which is the control parameter encoding the progression through mitosis (10); (**B**) the probability $\overline{p}$ for a force generator to be pulling; (**C**) the number of astral microtubules (MTs) contacting the cortex in the posterior-most crescent (green) and the number of engaged f.g. in this same region (blue); (**D**) the cortical force in pN exerted by these force generators on the posterior centrosome projected on the anteroposterior (AP) axis; and (**E**) the posterior displacement subsequently obtained. The parameters used are listed in Table S5. Dashed lines represent the results of the initial model that only accounts for a temporal control of pulling forces, while solid lines correspond to the full-expanded model that combines the positional switch through microtubule dynamics on top of the temporal control through force generator dynamics (Suppl. Model).

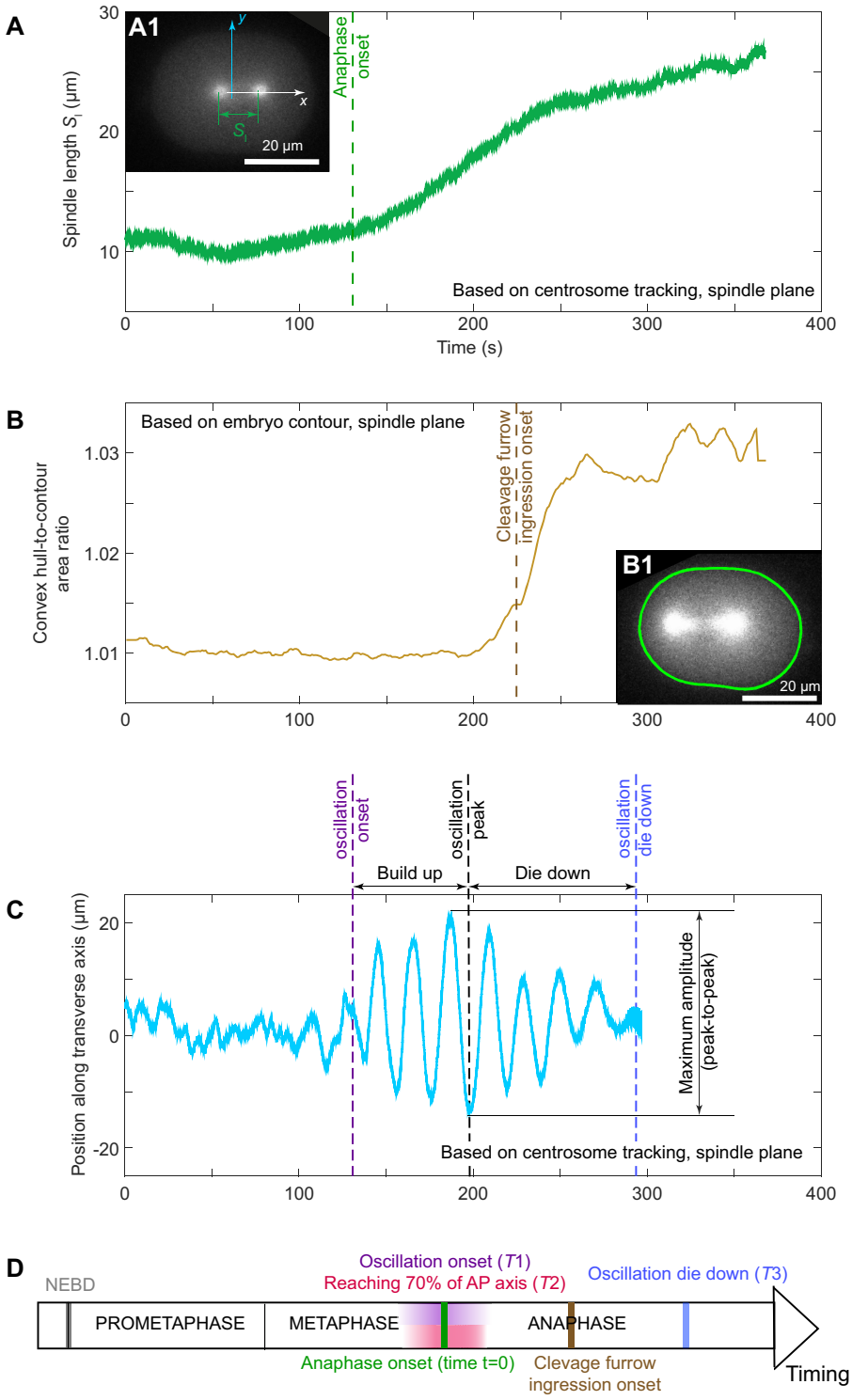

Figure S4: Landmarks used to set reference times and oscillation characteristics.
C. elegans centrosome trajectories and embryo shapes were measured at the spindle plane by viewing either the YFP::α-tubulin-labeled microtubule strain (inset **B1**) or the GFP::γ-tubulin-labeled centrosome strain (inset **A1**). (**A**) The spindle length was measured as the distance between the two centrosomes. Anaphase onset (dashed line) was defined as the inflection point towards a steeper increase in spindle length (16). (**B**) The ratio of the convex contour to the real contour is used to measure the convexity of the embryo contour (inset B1,

Suppl. Methods) and plotted across time. The cleavage furrow ingression timing (dashed line) is set as the inflection point in the convex hull-to-contour ratio steep increase. (**C**) Position of the posterior centrosome along the transverse axis of the embryo. The timings for the oscillation onset, peak amplitude, and die down are delineated. The vertical arrow indicates the maximum amplitude measurement (i.e. peak-to-peak distance in consecutive extrema). (**D**) A timeline highlights the timing of some key events during *C. elegans* mitosis whose values are displayed in Table 1 and Fig. 5BD: NEBD in orange; oscillation onset (referred as *T*1 in Table 1) in purple; oscillation die down (*T*2) in blue; time when posterior centrosome reaches the position of 70% of the embryo length (*T*3) in red; anaphase onset timing in green; and cleavage furrow ingression onset in brown. The color gradients indicate the possible variable timings since they are not constrained, as revealed by *RNAi* and mutant investigations.

Para-meter	Value	Description and Estimate
Initial model parameters		
N	50 (38 for the initial model)	Number of force generators per half cortex (9) (identical on both sides (8)). N = 38 when simulating the initial tug-of-war to ensure a similar posterior displacement as in the expanded model, all other parameters remaining similar.
K	5 μN/m	Centering spring stiffness. Same order of magnitude as (16, 28).
Γ	140 μN.s/m	Damping due to microtubule network (14) and cytoplasm viscosity along the transverse axis (28). Used to model oscillations only.
k_{on}^{post}	3 s^{-1}	Fixed force generator attachment rate (on-rate) on the posterior side, used only in the initial model.
k_{on}^{ante}	2 s^{-1}	Fixed force generator attachment rate (on-rate) on anterior side, used only in the initial model; its anterior value being lower than posterior to encode the polarity (8).
x_{ante}	42%	Fixed anterior centrosome position (in % of embryo length), corresponding to the experimental position at anaphase onset.
f_c	1.5 pN	Force generator detachment rate sensitivity to force (10).
f'	3 μN.s/μm	Slope of the force generator-force velocity relation (10).
$\bar{f}$	6 pN	Force generator stall force (10).
η	$\langle\lvert\eta\rvert\rangle = 0$ $\langle\lvert\eta\rvert^2\rangle = 0.1\delta(t)$	Stochastic noise modeling the binding and unbinding of force generators (10).
(Full) Expanded model parameters		
a	24.6 μm	Embryo half-length (along the AP axis), measured in this study.
b	15.75 μm	Embryo half-width (transverse to the AP axis), measured in this study.
M	3000	Number of microtubules emanating from each centrosome (22, 29).
α	2.15 μm^{-1}	Microtubule dynamics parameter, corresponding to known growing/shrinking rates (12, 15) and cortex residence time τ = 1.25 s (this work and (12)).
x_0^{post}	70%	Position of the boundary of the active region in posterior embryo half (in % of embryo length) (13).

Parameters for simulating posterior displacement		
Γ	300 μN.s/m	Damping due to microtubule network (14) and cytoplasm viscosity along the AP axis (28).
x_0^{ante}	40%	Position of the boundary of active force generator region in anterior embryo half (in % of embryo length) based on force distribution (9).
λ	0.5	Weakening factor of anterior forces to account for spindle pole uncoupling during elongation (30).
$\overline{k_{off}^{0}}$	4 s^{-1}	Force generator off-rate at the metaphase to anaphase transition, estimated from (8).
$\overline{k_{off}^{\infty}}$	2 s^{-1}	Final force generator off-rate (8).
$\overline{k_{off}^{init}}$	10 s^{-1}	Initial force generator off-rate. Time-dependent detachment rate (off-rate) $\overline{k_{off}(t)}$ varies following a sigmoid (10).
β_{post}	15	Affinity factor in posterior half of the cortex to account for the increased on-rate (8). Set to have a number of active force generators in the range of 10 to 100 and twice larger in posterior than in anterior (9).
β_{ante}	7.5	Affinity factor in anterior half of the cortex to account for the on-rate anteroposterior imbalance (8).
$\widehat{k_{on}}$	0.025 s^{-1}	Amplitude of the force generator attachment rate to the microtubule in the expanded model (Suppl. Model).

Table S5: Parameters used for modeling and simulations.
Parameters used to calculate the number of engaged force generators with the expanded model and to simulate the posterior displacement using the full-expanded model. The estimates were similar to the initial model if applicable or based on experimental results cited in the rightmost column.

Supplemental Methods to
"Microtubule feedback and LET-99-dependent control of pulling forces ensure robust spindle position."

"Landing" assay: Pipeline to measure microtubule contact densities and dynamics at the cortex

Choosing the labeling

Two main strategies could be envisaged to investigate microtubule dynamics (31): the labeling of growing microtubule ends with EB homolog proteins, and the labeling of the entire microtubule using tubulin tagged with fluorescent proteins, thus marking polymerizing and depolymerizing microtubules. Here, we chose the second option by using nematode strains with YFP::α-tubulin and GFP::β-tubulin transgenes for *Caenorhabditis elegans* and *Caenorhabditis briggsae* embryos, respectively. It allowed us to measure the duration of the residence of microtubules at the cortex, disregarding whether they were growing, shrinking or clamped in any of these two states. Dynein, which is required for the pulling forces that position the spindle (4), was indeed reported to also cause such a "residing state" *in vitro* (32). By labeling the microtubules in their whole, we could relate microtubule cortical contacts and spindle positioning, in particular posterior displacement during anaphase using modeling.

Characteristic measured (mean ± s.e.m.)	γ-tubulin labeling (N = 39, 23ºC)	α-tubulin labeling (N = 8, 23ºC) p for Student's t-test
Maximum oscillation amplitude (posterior) (% of embryo width)	19.43 ± 0.09	16.79 ± 0.51 p = 0.088
Maximum oscillation amplitude (posterior) (µm)	6.14 ± 0.03	5.54 ± 0.17 p = 0.224
Oscillation die down (s, from anaphase onset)	116.5 ± 0.3	115.08 ± 1.72 p = 0.774
Oscillation duration (s)	121.62 ± 0.49	121.88 ± 3.79 p = 0.980
Maximum oscillation peak (posterior) (s, from anaphase onset)	47.1 ± 0.3	43.36 ± 3.50 p = 0.688
Embryo length (µm)	49.23 ±0.07	48.23 ± 0.41 p = 0.39
Embryo width (µm)	31.53 ± 0.03	33 ± 0.14 p = 0.003

In this perspective, we checked that the α-tubulin overexpression in the *C. elegans* strain used for the "landing" assay was not resulting in any unexpected phenotypes by investigating the trajectories of the centrosomes and the amplitudes of their oscillations, the latter being a sensitive read-out of the pulling forces (10). To do so, we compared YFP::α-tubulin microtubule-labeled strain with the GFP::γ-tubulin centrosome-labeled strain that is the reference strain for spindle positioning investigations. We observed no significant difference either in the posterior and anterior centrosome trajectories along the anteroposterior (AP) axis throughout mitosis (Fig. S1A-B in the Supporting Material), or in posterior centrosome oscillation maximum

amplitude or timings (Table above). We concluded that the α-tubulin labeling does not perturb the centrosomal oscillation phenotype and that we could safely build our model based on experiments performed in strains displaying similar features.

Imaging of microtubule contacts at the cortex

We imaged *C. elegans* or *C. briggsae* one-cell embryos at the cortex plane in contact with the glass slide (Fig. 1D), viewing from the nuclear envelope breakdown (NEBD) until the end of cell division. We did our utmost to preserve the embryo shapes. The thickness of the perivitelline space (33) therefore meant we had to use spinning disk microscopy rather than TIRF. Cortical microtubule contact images were recorded using on a LEICA DMI6000 / Yokogawa CSU-X1 M1 spinning disc microscope, using an HCX Plan Apo 100x/1.4 NA oil objective. Illumination was performed using a white-light Fianium laser filtered around 514 nm in a homemade setup (17), sold by Leukos (Limoges, France). To account for the fast speed of microtubule dynamics at the cortex, images were acquired at an exposure time of 100 ms (10 Hz framerate) using an ultra-sensitive Roper Evolve EMCCD camera and the MetaMorph software (Molecular Devices) without binning. During the experiments, the embryos were kept at 23°C. To image embryos at the cortex, we typically moved the focus to 12 to 15 µm below the spindle plane (Fig. 1D).

Preprocessing of the cortical images

Since microtubule tubulin spot signals were very weak at the cortex (Fig. 1A), we denoised the images to increase the signal-to-noise ratio (Fig. 1B). This noise reduction usually relies on the assumption that the noise is non-correlated in space and time and that it follows a Gaussian or Poisson distribution over space or time. Along this line, we opted for Kalman filtering/denoising (18), setting the gain to 0.5, and the initial noise estimate to 0.05 performing in time and not requiring hypothesis in space.

Automated tracking of YFP::α-tubulin fluorescent spots at the cortex

Since the signal-to-noise ratio is low, we classified spots as microtubule contacts when they reside for a few images and set to use tracking to enforce this condition. Because of the large number of tracks present at the cortex, we looked for an algorithm with powerful track detection and segment linking capabilities. We opted for u-track (19), using the parameters below:

Detection	
Gaussian standard deviation	1.4
Alpha-value for initial detection of local maxima	0.08
Rolling window time-averaging	3
Iterative Gaussian mixture-model fitting	0
Tracking	
Maximum gap to close	5
Merge split	0
Minimum length of track segments from first step	3
Cost function frame-to-frame linking	
Flag for linear motion	1

Allow instantaneous direction reversal	1
Search radius lower limit	1
Search radius upper limit	3
Standard deviation multiplication factor	3
Nearest neighbor distance calculation	1
Number of frames for nearest neighbor distance calculation	4
Cost function close gaps	
Flag for linear motion	1
Search radius lower limit	1
Search radius upper limit	3
Standard deviation multiplication factor	3
Nearest neighbor distance calculation	
Number of frames for nearest neighbor	4
Penalty for increasing gap length	1.5
Maximum angle between linear track segments	30

Measuring microtubule residence time at the cortex and consistency check

We calculated the histogram for the durations of microtubule contacts at the cortex. We used a bin size of 100 ms, equal to the image acquisition time. The exponential fit of the histogram yielded a microtubule lifetime (Fig. 1E), consistent with previous work (12). Indeed, the duration of a microtubule contact at the cortex is limited by its switching to de-polymerization (catastrophe), which is a first order stochastic process. Furthermore, the increasing count of microtubule cortical contacts at anaphase (Fig. 1FG, Fig. 2A,D) was consistent with the increased microtubule nucleation rate previously reported (15). We determined the residence times of astral microtubule contacts at the cortex in the different depletion conditions performed to challenge our full-expanded model. Except for *par-3(RNAi)* treatment, which led to a lifetime slightly above the control (p-value = 0.03), we did not notice any significant differences in the residence times of these 4 conditions compared to controls (Fig. S1C).

Validation of the microtubule contact analysis at the cortex

To gain confidence in the processing beyond the consistency, we validated the u-track parameters by analyzing fabricated fluorescence images of known dynamics (Fig. S1D-F), which mimic our cortical images (34). We simulated stochastic trajectories of particles (Fig. S1D) that displayed a limited random motion: $x_{i,j}(t+1) = x_{i,j}(t) + \xi\sqrt{2Dt}$, where $x_{i,j}(t)$ represents the coordinates in two dimensions at time t, ξ is a random number and D is the diffusion coefficient. The duration of the tracks (length) was sampled from an exponential distribution. The intensity was set similar to experimental levels and encoded by the quantum yield parameter (Qyield). We then plotted the instantaneous positions and applied a Gaussian blur filter to mimic the effect of the point-spread function in fluorescence microscopy. We mimicked the background noise by adding at each pixel a sampling of a Gaussian distribution normalized to ε, with formula reading $A_{\text{noisy}} = A + \varepsilon M$ and corresponding to a signal-to-noise ratio max(A)/

ε (Fig. S1E). This simulation provided a realistic scenario to test the image-processing pipeline. Details of the parameters used for simulation can be found below. We were able to get very good matching of duration distributions by plotting values used to generate the simulated tracks and the ones recovered through analyzing fabricated images (Fig. S1F). This validated our microtubule contact tracking approach.

Image size	256 x 256
Duration	3000 frames (300 s)
Density of particles (tracks)	1 particle /μm^2
QYield	0.61
Pixel size	0.139 nm
Sampling rate	0.1 s
PSF type	Gaussian
PSF size	0.244 µm
Bits	12
Diffusion coefficient	0.002 μm^2/s
Background noise standard deviation	0.5
Mean track lifetime	1 s

Computing microtubule contact densities at the cortex ("landing" assay)

The "landing" assay consisted in measuring the cortical microtubule contacts (Fig. 1D) during the different phases of mitosis. The section of embryo contacting the cover-slip was divided into ten regions of equal width along its long axis (AP axis). The u-track algorithm allowed us to follow the microtubule contacts at the cortex frame-by-frame, and to have access to their trajectories (19). We segmented the embryo cytoplasm so we could track embryo shape changes throughout cell division using the active contour algorithm (20), obtaining data on how the lengths and areas of the embryos evolved during mitosis. To increase confidence in the measurements, we split the contacting area into 10 regions and counted the microtubules contacting the cortex in these regions along the embryo length (Fig. 1D) for each frame acquired at a frequency of 10 Hz and divided by the corresponding area to compute the densities. To reinforce certainty, the densities of the microtubule contacts were block-averaged over time for 10 s. Indeed, since the microtubules reside briefly at the cortex (≈1 s), we imaged at a high frequency. However, the density modulation occurs at slower timescale allowing us to perform such a running average. Finally, we used the onset of cytokinesis cleavage furrow ingression (see below and Fig. S4B) as a temporal reference for the alignment of the microtubule cortical contact density maps over the embryos, and then averaged to get the final density map.

Timing of cytokinesis cleavage furrow ingression onset to overlay centrosome trajectories to microtubule cortical contact density

We determined the timing of the onset of cleavage furrow ingression (CFI) at the spindle plane (embryo's middle) and at the cortex plane by taking advantage of the dyed cytoplasmic fraction to detect the embryo contours. These contours were obtained through the active contour algorithm (20). We then set the onset of cleavage furrow ingression to equal the fast increase in the ratio of the convex area of the embryo to the area enclosed by its contour (Fig. S4B). In practice, we set the CFI onset timing when the ratio grew above 1.012. Then, to align

density maps with centrosome tracks (the latter being aligned on anaphase onset), we calibrated the average time between anaphase (starting at the inflection point during spindle elongation (16) (Fig. S4A)) and the CFI onset. We then used this time difference to estimate anaphase onset at the cortex plane from CFI onset measurements. Matching the anaphase onset timings from the "landing" and "centrosome-tracking" assays, we could overlay these two different sets of experiments (Fig. 2A,D).

Residence time of the microtubules at the cortex

For each embryo, we plotted the histogram of the track durations of the microtubule contacts at the cortex and fitted it by a mono-exponential function. We recovered a lifetime characterizing the exponential decay and then averaged the exponential decay lifetimes over the embryos of a given condition. Results are reproduced in Fig. S1C.

Supplemental movie legends to
"Microtubule feedback and LET-99-dependent control of pulling forces ensure robust spindle position."

Movie S1: Spindle positioning in a *C. elegans* control embryo.
Movie of a *Caenorhabditis elegans* one-cell embryo imaged at the spindle plane upon *RNAi* using the empty L4440 vector. Centrosomes are labeled by GFP::γ-tubulin and embryo radii are equal to 48.7 μm and 31.3 μm. The movie was accelerated to 10x real-time. Anaphase onset was measured at time 26.05 s in movie' s time. Stills extracted from this movie are reproduced in Fig. S2E in the Supporting Material, top row.

Movie S2: Spindle positioning in a reduced-microtubule-nucleation embryo.
Movie of a *C. elegans* one-cell embryo imaged at the spindle plane during mitosis upon *spd-2(RNAi)* treatment. Centrosomes are labeled by GFP::γ-tubulin and embryo radii are equal to 49.0 μm and 31.9 μm. The movie was accelerated to 10x real-time. Anaphase onset was measured at time 22.15 s in movie' s time. Stills extracted from this movie are reproduced in Fig. S2E, bottom row.

Supplemental Model to "Microtubule feedback and LET-99-dependent control of pulling forces ensure robust spindle position."

Hélène Bouvrais[*,1,2], Laurent Chesneau[1,2], Sylvain Pastezeur[1,2], Danielle Fairbrass[1,2], Marie Delattre[3], and Jacques Pécréaux[*,1,2]

[1]CNRS UMR 6290, F-35043 Rennes, France.
[2]University of Rennes 1, UEB, SFR Biosit, School of Medicine, F-35043 Rennes, France
[3]Laboratory of Molecular Biology of the Cell, École Normale Supérieure de Lyon, CNRS, F-69363 Lyon, France

October 4, 2018

[*]To whom correspondence should be addressed: helene.bouvrais@univ-rennes1.fr, jacques.pecreaux@univ-rennes1.fr

Abstract

During the asymmetric division of the nematode zygote, the mitotic spindle undergoes anaphase oscillations. This rocking is caused by cortical pulling forces exerted on astral microtubules, which also contribute to positioning and elongating the spindle. Therefore, these oscillations are instrumental in deciphering the mechanics of cell division, in particular the contribution of microtubules and force generators. By modeling them, we previously revealed that oscillation build-up and die down were regulated by the dynamics of force generator, likely dynein. Using agent-based simulation, Kozlowski and colleagues highlighted the role of astral microtubule dynamics. We propose here a modeling of these both regulations by linear stochastic differential equation. It suggests that anaphase oscillation onset is mostly controlled by the position of the posterior centrosome with respect to the region where force generators are active. In contrast, oscillation die down is mostly controlled by mitotic progression through force generator dynamics. We recently confirmed experimentally these findings through *in vivo* measures during the first division of the nematode embryo. Because the pulling forces also cause the posterior displacement of the spindle, their positional control creates a feedback. By simulating posterior centrosome position through mitosis, we suggest that this feedback loop provides robustness to the details of force generator count and dynamics. In contrast, we propose that the position of the active region boundary, dependent on the polarity of the cell, sets the final spindle position. This is highly relevant since the spindle position at the end of an asymmetric division ensures the correct distribution of cell fate determinants.

Contents

1 Introduction

During the division of nematode zygote, the spindle undergoes a complex choreography. Firstly, during prophase, the pronuclei-centrosome complex (PCC) moves from posterior half of the embryo to its center, during the so-called centering phase (35) and concurrently the two centrosomes align along the anteroposterior (AP) axis. We previously found, in contrast to *Caenorhabditis elegans* embryo, that this displacement was a bit excessive in *C. briggsae* reaching a slightly more anterior position, a phenomenon called *overcentration* (7, 27). The consequence is a delay in spindle posterior displacement for this species with respect to *C. elegans*. Interestingly, the same proteins that cause the anaphase posterior displacement are needed for this (7), namely the trimeric complex GPR-1/2^{LGN}, LIN-5^{NuMA} and dynein (4). Later on, during prometaphase and metaphase, the spindle is maintained in the middle by centering forces that are independent of GPR-1/2 and may be caused by microtubule pushing against the cell cortex (16). Finally, during late metaphase and anaphase, GPR-1/2-dependent cortical pulling forces become dominant, displace the spindle posteriorly, make it oscillate, and contribute to its elongation (9, 10, 23).

We aim here to complement our previously published "tug-of-war" model (10, 11), later called initial model, which was mainly focused on the dynamics of cortical force generators (f.g.), by including the dynamics of astral microtubules (MTs). Indeed, we mapped the microtubule contacts at the cortex and revealed that they mostly concentrated in cortical regions close to the centrosomes (see main text). In consequence, the position of the centrosomes, as microtubule organizing centers (MTOC), regulates the quantity of engaged force generators pulling on astral microtubules and in turn anaphase oscillation of spindle poles and posterior displacement of the spindle.

Firstly, focusing on the oscillation onset, we expanded our initial model of spindle oscillation to account for microtubule dynamics. We detailed the expanded model and then explored how this novel positional regulation combines with the one by force generator processivity previously reported (10). Secondly, through a stochastic simulation approach, we looked at the feedback loop created between the position of the posterior centrosome and the pulling forces contributing to spindle displacement.

2 Modeling the positional switch on oscillation onset

2.1 Quantity of microtubules reaching the posterior-most crescent of active force generators

Recent work suggested that force generators would be active only on a posterior cap instead of the whole posterior half cortex of the embryo, so-called the posterior-most crescent or the active region (13). This means that only the microtubules hitting the posterior-most crescent of the cortex would contribute to spindle displacement by binding to active force generators. We thus calculated the number of microtubules reaching this active region of the cortex.

2.1.1 Modeling hypotheses and microtubule dynamics parameter estimates

We set to explore whether the number of microtubules reaching the cortex, assumed to be in excess during anaphase (10, 11), could be limiting prior to oscillation onset. Key to assess this

possibility was an estimate of the total number of microtubules and their dynamics. Based on previously published experiments, we assessed the following microtubule related parameters:

- **Total number of microtubules.** To assess the number of microtubule nucleation sites at the centrosome (CS), we relied on electron microscopy images of the centrosomes (29), which suggested 3000 or more microtubules emanating per centrosome. This order of magnitude was previously proposed by O'Toole and collaborators (22). More specifically in the figure 3 of (29), authors provide a slice of about 0.85 μm thick (as estimated from video 8) displaying 520 astral microtubules, while centrosome diameter was estimated to 1.5 μm. Only a slice of centrosome was viewed in this assay, so that the number of microtubule nucleation sites per CS was extrapolated to a least 1800 considering the centrosome as a whole sphere. In this work, we set the number of microtubules to $M = 3000$. Variation of this number within the same order of magnitude does not change our conclusions.

- **The microtubules are distributed around each centrosome in an isotropic fashion.** We hypothesized an isotropic distribution of microtubules around each centrosome following (14). This was also suggested through electron microscopy (29).

- **Free-end catastrophes are negligible.** With the above estimate of the microtubule number and considering a microtubule growing speed in the cytoplasm $v^+ = 0.67$ μm/s (15) and a shrinking one $v^- = 0.84$ μm/s (12), we could estimate that about 70 microtubules reach the cell periphery (assumed to be at 15 μm from the centrosome) at any moment and per centrosome, if the free-end catastrophe rate is negligible. This estimate appears consistent with the instantaneous number of force generators in an half-cortex, estimated between 10 and 100 (9).

  Furthermore, it was recently proposed that the catastrophe rate could be as high as 0.25 s^{-1} in the mitotic spindle (29). On the one hand, this might be specific to this organelle since the spindle is much more crowded than the cytoplasm. On the other hand, these authors proposed a total number of microtubules two to three folds larger than our estimate. We asserted that our conservative estimate of the microtubule quantity combined with the negligible free-end catastrophe resulted in similar modeling results, with the advantage of the simplicity over a full astral microtubule model. In other words, we focused on the fraction of astral microtubules not undergoing free-end catastrophe, which was the only one measurable at the cortex.

  We next wondered whether the assumption of negligible free-end catastrophe is consistent with our measurement of microtubule contact density at the cortex. After (29), the vast majority of microtubules emanating from the centrosome are astral: we thus assumed that the kinetochore and spindle microtubules were negligible in this estimate. Focusing on metaphase and with a residence time of microtubule ends at the cortex $\tau = 1.25$ s (12) (see main text), this led to about 100 microtubules contacting the cortex per centrosome, at any given time. Using our "landing" assay (see main text), we could estimate the number of contacts in the monitored region at any given time to 5 microtubules. Extrapolating this to a whole centrosome and assuming the isotropic distribution of astral microtubules (§2.1.2), we found 26 cortical contacts of microtubules at any time in metaphase. Although a bit low, likely because of the conservative parameters of the image processing that could led to missing some microtubules, this

experimental assessment was consistent with the theoretical estimate based on our hypotheses. Furthermore, it was also consistent with the measurement done by (28). In contrast, a non negligible catastrophe rate would have dramatically reduced that number of contacts at any given time. We concluded that free-end catastrophe rate was safely negligible.

- **No microtubule nucleation sites are left empty at the centrosomes** This is a classic hypothesis (14), recently supported by electron microscopy experiments (29).

2.1.2 Microtubule dynamics "measure" the centrosome-to-cortex distance.

Probability for a microtubule to be at the cell cortex Because microtubules spend most of their "lifespan" growing to and shrinking from the cortex, the distance between the centrosome and the cortex limits the number of microtubules residing at the cortex at any given time. We could thus summarize microtubule dynamics in a single parameter α by writing the fraction of time spent by a microtubule at the cell cortex:

$$q = \frac{\tau}{\frac{d}{v^+} + \frac{d}{v} + \tau} = \frac{1}{1+\alpha d} \quad \text{with } \alpha = \frac{1}{v^+\tau} + \frac{1}{v^-\tau}, \tag{1}$$

where d is the distance from the centrosome (MTOC) to the cortex (estimated to typically $d = 15\ \mu$m, *id est* about half of the embryo width). We then found $\alpha = 2.15 \times 10^6\ \mathrm{m}^{-1}$ using the above microtubule dynamics parameters. This meant that the microtubule spent $q = 3\%$ of its time at the cortex and the remaining time growing and shrinking. This fraction of time spent residing at the cortex was consistent with the estimate coming from investigating the spindle centering maintenance during metaphase (16).

Range of variations in the microtubule contact densities at the cortex. The nematode embryo shape is close to an ellipsoid. Therefore, the centrosome displacement can vary the centrosome-to-cortex distance by 1.5 to 2 fold. We wondered whether the microtubule dynamics were so that one could observe significant variations in cortical microtubule-residing probabilities q. We estimated this sensitivity through the ratio ρ of the probability of reaching the cortex when the centrosome was at its closest position d_1 (set to half of the embryo width, i.e. the ellipse short radius) divided by the probability when it was at its furthest position d_2 (chosen as half of the embryo length, i.e. the ellipse long axis).

$$\rho = \frac{1+\alpha d_2}{1+\alpha d_1} \tag{2}$$

This curve had a sigmoid-like shape with $\lim_{\alpha\to 0} \rho = 1$ and $\lim_{\alpha\to\infty} \rho = d_2\,/d_1$.

Using our measurement of microtubule contact distribution at the cortex (see main text), we calculated an experimental estimate of this sensitivity parameter, $\rho_{exp} \simeq 2$. On model side, because the experimental "landing" assay did not enable us to view the very tip of the embryo (Fig. M1), we compared the sensitivity ratio calculated from the density map with a theoretical one that did not use the half embryo length as maximum distance but the largest distance effectively measurable. For untreated embryos viewed at the spindle plane, the measured embryo length was $2a = 49.2\ \mu$m, while imaging at the cortex, the length along the AP axis (denoted with bars) was $2\bar{a} = 38.0\ \mu$m for the adhering part to the coverslip.

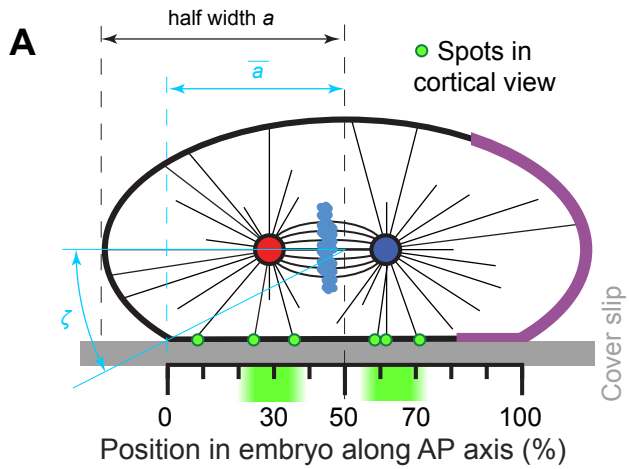

Figure M1: **Experimental setup for viewing microtubule (MT) contact density at the cell cortex.** The scale represents the 10 regions along the anteroposterior (AP) axis used for analysis (see main text). Red and blue disks represent the anterior and posterior centrosomes, respectively, and the light blue clouds are the chromosomes. Microtubules emanating from the centrosomes are thin black lines. The posterior-most crescent where the active force generators are located is the cortical purple region.

We could calculate the truncation of the ellipse due to the adhesion through the polar angle $\zeta = \arccos(\bar{a}/a)$ of the boundary of the adhering region. We obtained $\zeta = 39.4°$ which corresponded to a spindle plane to flattened cortex distance of 10 μm, using a parametric representation of the ellipse. During metaphase (set as the two minutes preceding anaphase onset), when the spindle is roughly centered (16), the average spindle length was 11.8 μm (N = 8 embryos). The furthest visible region was thus at $d_2 = 16.5$ μm while the closest one was at $d_1 = 10$ μm, leading to a sensitivity ratio $\rho = 1.62$ consistent with the microtubule cortical contact density ratio observed *in vivo* for *C. elegans*. We concluded that microtubule dynamics in *C. elegans* enable the read-out of the posterior centrosome position through the probability of microtubules to be in contact with the cell cortex.

2.1.3 Number of microtubules reaching the cortex

We set to estimate the variation of the total number of astral microtubule contacts emanating from a single centrosome versus the position of this centrosome along the AP axis. We worked in spherical coordinates (r, θ, ϕ) centered on the posterior centrosome that displayed a slow posterior displacement assumed to be a quasi-static motion, with zenith pointing towards posterior. We denoted θ the zenith angle and ϕ the azimuth (Fig. M2A). We calculated the probability of a microtubule to reach the cortex in the active region, represented as $\theta \in [0, \theta_0]$ and $\phi \in [0, 2\pi[$. We integrated over the corresponding solid angle and the number of microtubules reaching the cortex $\mathcal{M}(\mathcal{S}, \alpha)$ came readily (Fig. M2B):

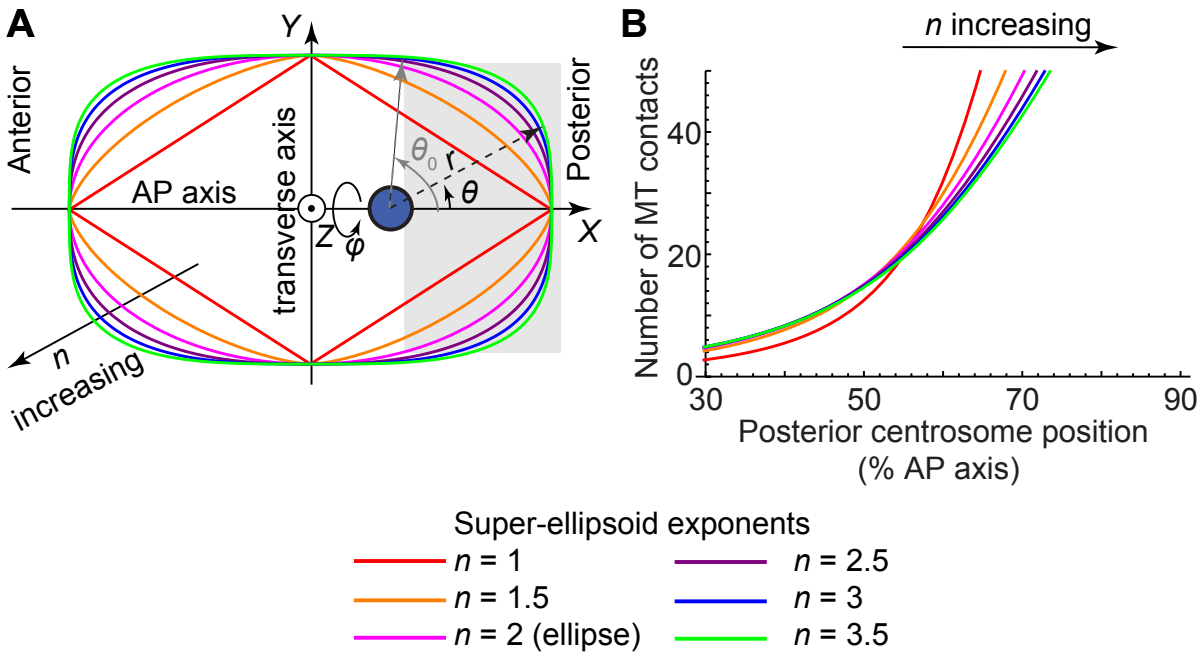

Figure M2: **The regime change in the microtubule contacts is preserved after super-ellipsoid modeling of embryo shape using various exponents.** An embryo shape was modeled by super-ellipsoids of the variable n (long axis 24.6 μm and short axis 15.75 μm), with $n = 2$ representing the ellipse. (A) Super-ellipses with the exponent n set to 1 to 3.5. The centrosome was positioned at 67% of the anteroposterior (AP) axis and is a blue disk. Cartesian axes (X, Y, Z) are indicated as well as spherical coordinates centered on the centrosome. The active region is grey, and its boundary was set to 70% of embryo length and at angle in centrosome-centered spherical coordinates. (B) Number of microtubules contacting the active region versus the position of the posterior centrosome along the AP axis, which is shown as a percentage of embryo length. Embryo shape was modeled using super-ellipsoids of revolution based on the super-ellipses plotted in A, and the parameters used are listed in Table S5 in the Supporting Material.

$$p\left(\mathcal{S}, \alpha, \theta, \phi\right) = \frac{1}{1 + \alpha\, r_{\mathcal{S}}\left(\theta, \phi\right)} \sin\left(\theta\right) \tag{3}$$

$$P\left(\mathcal{S}, \alpha\right) = \int_{\theta=0}^{\theta_0} \int_{\phi=0}^{2\pi} p\left(\mathcal{S}, \alpha, \theta, \phi\right) \mathrm{d}\,\phi\, \mathrm{d}\,\theta \tag{4}$$

$$\mathcal{M}\left(\mathcal{S}, \alpha\right) = M\,/4\pi\; P\left(\mathcal{S}, \alpha\right) \tag{5}$$

where $r_{\mathcal{S}}\left(\theta, \phi\right)$ is the distance centrosome-to-cortex in polar coordinates centered on the centrosome, dependent upon the shape of the cortex $\mathcal{S}$ and the boundary of the active force generator region θ_0 (Fig. M1). We observed a switch-like behavior as the posterior centrosome went out of the cell center and closer to the posterior side of the embryo (Fig. M2B).

2.2 Towards the expanded tug-of-war model

In the initial model (10, 11), we made the assumption that the limiting factor was the number of engaged cortical force generators, while in comparison the astral microtubules were assumed to be in excess. It resulted that oscillations were driven by the force generator quantity and dynamics. In the linearized version of the initial model, the persistence of force generators to pull on microtubules (i.e. their processivity) mainly governed the timing and frequency of the oscillations, while the number of force generators drove the amplitude of oscillations (10). However, since the number of microtubules reaching the cortex could be limiting (12), we expanded the initial model of anaphase oscillations to account for this possible limitation.

2.2.1 The initial model

We provide here a brief reminder of the initial tug-of-war model (10). It featured cortical force generators exhibiting stochastic binding to and detaching from microtubules at rates k_{on} and k_{off} ($\overline{k_{off}}$ being the detachment rate at stall force $\bar{f}$), respectively. The force generators were assumed to act close to stall force. The mean probability for a force generator to be pulling on a microtubule then reads $\bar{p} = k_{on} \big/ \left(k_{on} + \overline{k_{off}}\right)$. The active force generators were distributed symmetrically between the upper and lower posterior cortices but asymmetrically between anterior and posterior cortices (9). In the model, we also included two standard properties of the force generators: firstly, a force-velocity relation $f = \bar{f} - f'\,v$, with f the current force, v the current velocity, and f' the slope of the force velocity relation ; secondly, a linearized load dependent detachment rate $k_{off} = \overline{k_{off}}\left(1 - \frac{\bar{f}-f}{f_c}\right)$, with f_c the sensitivity to load/pulling force, assuming that force generator velocity was low, i.e. they acted close to the stall force (10). We finally denoted Γ the passive viscous drag, related in part to the spindle centering mechanism (14, 16, 28), and $\bar{N}$ the number of available force generators in the posterior-most cortex.

A quasi-static linearized model of the spindle posterior displacement reads:

$$I(\bar{p})\ddot{y} + \left(\Gamma - \Xi(\bar{p})\right)\dot{y} + Ky = 0, \tag{6}$$

with

$$\Xi(\bar{p}) = 2\bar{N}\left\{\frac{\bar{f}}{f_c}\bar{p}\left[(1-\bar{p}) - \frac{f_c}{\bar{f}}\right]\right\} f', \tag{7}$$

and

$$I(\bar{p}) = 2\bar{N}\left\{\frac{\bar{f}}{f_c}\bar{p}\,(1-\bar{p})\right\} f'\frac{\bar{p}}{k_{on}}, \tag{8}$$

with K the centering spring stiffness and I the inertia resulting from stochastic force generator binding and unbinding. The spindle oscillations develop when the system becomes unstable, meaning when the negative damping $\Xi(\bar{p})$ overcomes the viscous drag Γ.

2.2.2 Evolution of the initial model to account for the polarity encoded through force generator on-rate

When we designed the initial model, it was known that the spindle posterior displacement was caused by an imbalance in the number of active force generators (9), i.e. the number of force generators engaged in pulling on astral microtubules or ready to do so when meeting an

astral microtubule. However, the detailed mechanism building this asymmetry was elusive. We recently investigated the dynamics of dynein at the cell cortex (8) and concluded that the force imbalance rather resulted from an asymmetry in force generator attachment rate to the microtubule. This asymmetry reflects the asymmetric location of GPR-1/2 (6, 7). More abundant GPR-1/2 proteins at posterior-most cortex could displace the attachment reaction towards more binding/engaging of force generators. Therefore, to simulate the posterior displacement of the posterior centrosome (§3), we rather used the equations above (Eq. 6-8) with distinct on-rates between anterior and posterior sides and equal quantity of available force generators.

2.2.3 Number of engaged force generators: modeling the binding of a microtubule to a force generator

Force generator–Microtubule attachment modeling To account for the limited number of cortical anchors (10, 11), we modeled the attachment of a force generator to a microtubule (4) as a first order process, using the law of mass action on component quantity (24) and combined it to the equations of quantity conservation for force generators and microtubules. It corresponded to the pseudo-chemical reaction:

$$\text{Microtubule} + \text{Force}-\text{generator} \longrightarrow \text{MT—Force}-\text{generator}$$

and the equilibrium equation came readily:

$$K_a = \frac{N_{\text{microtubule–force-generator}}}{N_{\text{free-microtubule-at-cortex}}\, N_{\text{free-force-generator}}} \tag{9a}$$

$$N = N_{\text{Microtubule–force-generator}} + N_{\text{free-force-generator}} \tag{9b}$$

$$M = N_{\text{microtubule–force-generator}} + N_{\text{free-microtubule-at-cortex}} \tag{9c}$$

$$= \mathcal{M}\left(\mathcal{S}, \alpha\right) \tag{9d}$$

where N is the total number of force generators present in the active region.

We could relate the association constant K_a to our initial model (10) (§2.2.1) by writing

$$K_a = \begin{cases} \widehat{k_{on}} \,/\overline{k_{off}} \\ \\ \bar{p}\,/(1-\bar{p})\,/N_{\text{free-microtubule-at-cortex}} \end{cases} \tag{10}$$

with the on-rate $k_{on} = \widehat{k_{on}} N_{\text{free-microtubule-at-cortex}}$, and the off-rate $\overline{k_{off}}(t)$ thought to depend on mitosis progression. Time dependences were omitted for sake of clarity. It was noteworthy that k_{on}, used in the initial model as force generator binding rate (assuming microtubules in excess), became variable throughout mitosis in the expanded model as it depends on the number of free microtubule contacts at the cortex, thus on the centrosome position. In contrast, $\widehat{k_{on}}$ appeared constant in the expanded model representing the on-rate of the first order reaction above.

Related parameter estimate In modeling anaphase oscillation onset, we assumed that the off-rate dependence on mitosis progression was negligible (§2.2.7 and 3 for full model without this assumption). The positional switch modeled here led to a limited number of engaged force generators at oscillation onset. At this time, the force generator quantity just crossed the threshold to build oscillations (10) and we estimated that typically 70% of the force generators were thus engaged, consistent with the quick disappearance of oscillations upon progressively depleting the embryo from GPR-1/2 proteins. We observed that the oscillation started when the centrosome reached 70% of embryo length (Table S5). At that moment, 52 microtubules were contacting the cortex (§2.1.1). We set the total number of force generators to 50 and got a number of engaged ones consistent with previous reports (9). We thus estimated the association constant $K_a^0 \simeq 0.1$ (denoted with 0 superscript to indicate that we assumed negligible its variation throughout mitosis). In turn, we estimated $\widehat{k_{on}} \simeq 0.025\ \mathrm{s}^{-1}$ assuming that the detachment rate at that time was about $4\ \mathrm{s}^{-1}$ (8). If 70% of the force generators were engaged at oscillation onset, it would correspond to $k_{on} \simeq 0.375\ \mathrm{s}^{-1}$, thus comparable to the estimate of this parameter in the initial model (10).

Modeling the number of engaged force generators in the posterior-most crescent In mitosis early stages, when the spindle lays in the middle of the embryo (*C. elegans*) or slightly anteriorly (*C. briggsae*), both centrosomes are far from their respective cortex and thus the imbalance in active force generator quantity due to embryo polarity results in a slight posterior pulling force and causes a slow posterior displacement. The closer the posterior centrosome gets to its cortex, the larger the force imbalance (because more microtubules reach the cortex), and the posterior displacement accelerates to (potentially) reach an equilibrium position during metaphase resulting in a plateau in posterior centrosome displacement located around 70% of the AP axis. Once anaphase is triggered, the decreased coupling between anterior and posterior centrosomes results into a sudden imbalance in favour of posterior pulling forces so that the posterior displacement speeds up (see main text).

We quantitatively modeled this phenomenon by combining the law of mass action above (Eq. 9a) with the number of microtubules reaching the posterior crescent (Eq. 5) to obtain the number of engaged force generators in the posterior cortex as following:

$$\begin{aligned} &\mathcal{N}\left(\mathcal{M}\left(\mathcal{S},\alpha\right)\right) = N\frac{\phi-1}{\phi+1} \\ &\quad \text{with} \quad \phi = \zeta^- + \sqrt{1+\zeta^{-2}+2\zeta^+} \\ &\quad \zeta^\pm = K_a\left(\mathcal{M}\left(\mathcal{S},\alpha\right) \pm N\right) \end{aligned} \tag{11}$$

To challenge our expanded model, we tested the switch-like behavior in a broad range of association constants K_a (Fig. M3A). When the posterior centrosome was between 50% and 70% of embryo length, we observed that the number of engaged force generators was increased up to a threshold that enabled oscillations, consistently with (10). When the centrosome was posterior enough, practically above 70% of the AP axis, the number of engaged force generators saturated, suggesting that their dynamics were now the control parameters, as proposed in the initial model during anaphase. We also observed that a minimal binding constant was needed to reach the threshold number of engaged force generators required for oscillations. Interestingly, above this minimal K_a, further increase of the binding constant did

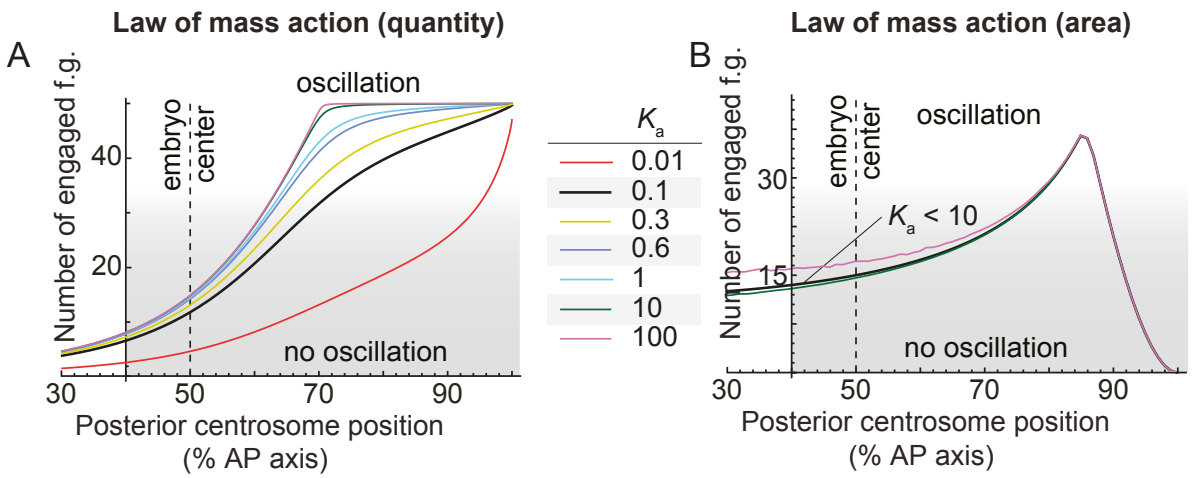

Figure M3: **Comparison of mass action law models using quantity and areal concentrations.** When varying the force generator–microtubule association constant K_a, graph of the number of engaged force generators (f.g.) versus the posterior displacement of the centrosome along the anteroposterior (AP) axis. For the centrosome positions above 60% of the AP axis, the number of engaged f.g. steeply increases, saturating above 70% and creating a switch-like behavior. Force-generator–microtubule binding was modeled by the law of mass action in: (A) quantity, with total number of force generators $N = 50$; and (B) areal concentration (§2.2.3), with $N = 500$. In both cases, we got similar numbers of engaged force generators between 10 to 100 that are consistent with experimental estimates (9) (§2.2.6). The parameters used are listed in Table S5. Grey shading indicates when the engaged force generator count was too low to permit oscillation (below threshold).

---

not alter significantly the positional switch (Fig. M3A). This suggested that this positional switch operates rather independently of the force generator processivity. This will be further discussed below (§2.2.7).

The positional switch is independent of the total number of force generators, as soon as this quantity is above a threshold As we previously suggested that the total number of force generators should not impact the positional switch (7), we calculated the corresponding prediction in our expanded model (Fig. S2B in the Supporting Material) and compared it with experimental prediction (Fig. S2C). The good match supports our expanded model. In modeling *gpr-1/2(RNAi)* through the total number of force generators N, we followed the common thought that asymmetry of active force generators was due to an increased total number of force generators on the posterior side.

We recently proposed that the asymmetry in active force generators could be an asymmetry of force generator association rate to form the trimeric complex that pulls on microtubules (8). GPR-1/2 presence would increase this on-rate. In our expanded model, a decreased on-rate (through *gpr-1/2(RNAi)*) would result in a decrease association constant K_a. Like is the previous case, above a certain threshold of K_a, the position at which oscillation starts was not significantly modified (Fig. M3A). In conclusion, independently of the details used to model the force imbalance consequence of the polarity (i.e. the total number or the on-rate), the mild depletion of GPR-1/2 experiment, causing a reduced number of active force generators,

supported our expanded model.

2.2.4 The change of regime in the number of microtubules reaching the cortex versus the centrosome position is independent of detailed embryo shape

The above results were obtained by assuming an ellipsoidal shape for the embryo (an ellipsoid of revolution around the AP axis, prolate or oblate). We wondered whether a slightly different shape could alter the result. We thus repeated the computation, modeling the embryo shape by a super-ellipsoid of revolution, based on super-ellipses (Lamé curves) (36) defined as:

$$\left|\frac{X}{a}\right|^n + \left|\frac{Y}{b}\right|^n = 1 \tag{12}$$

with a and b the half length and width, n the exponents, and (X, Y, Z) the cartesian axes with X along the AP axis (long axis), and positive values towards the posterior side. We obtained a similar switch-like behavior (Fig. M2). We concluded that the switch-like behavior was resistant to changes of the detailed embryo shape and thus performed the remaining investigations with an ellipsoid shape, for sake of simplicity.

2.2.5 Sensitivity analysis of the oscillation onset position to embryo geometry and microtubule dynamics

The expanded model offers a regulation of cortical pulling forces, as revealed by oscillation onset, by the position of the centrosome. We therefore investigated how the shape of the embryo could impact the switch. Indeed, various species of nematodes display different long and short axes, resulting in scale and eccentricity variations (37). In Fig. 4, we reported that embryo length has a reduced impact on the switch. In contrast, the embryo width is more influential over the switch (Fig. M4A). It is noteworthy that embryo length undergoes a stronger selection in genetic studies in comparison with embryo width (25).

Then, we investigated the sensitivity of the oscillation onset position to parameters describing embryo shape in a different representation. We found a robustness of the position of oscillation onset versus the eccentricity, i.e. variations in embryo length keeping area constant (Fig. M4CD), while embryo scale was more influential (Fig. M4B). This is perfectly consistent with the positional control, which measures the distances in units of microtubule dynamics (§2.1.2). Consequently, the position at which oscillation starts is highly dependent on microtubule dynamics (Fig. M4E).

2.2.6 Discussion: number- or density-limited force generator-microtubule binding

By writing the law of mass action in protein quantity (Eq. 9a), we assumed that the force generator-microtubule binding reaction was rate-limited but not diffusion-limited. We recently investigated the dynamics of cytoplasmic dynein (8) and observed that dynein molecules were abundant in cytoplasm, thus 3D diffusion combined to microtubule plus-end accumulation brought enough dynein to the cortex. Therefore, diffusion of dynein to the cortex was not likely to be a limiting factor in binding force generators to the microtubules. However, another member of the force-generating complex, GPR-1/2, essential to generate pulling forces (4, 9, 10), may be limiting. GPR-1/2 is likely localized at the cell cortex prior to assembly of

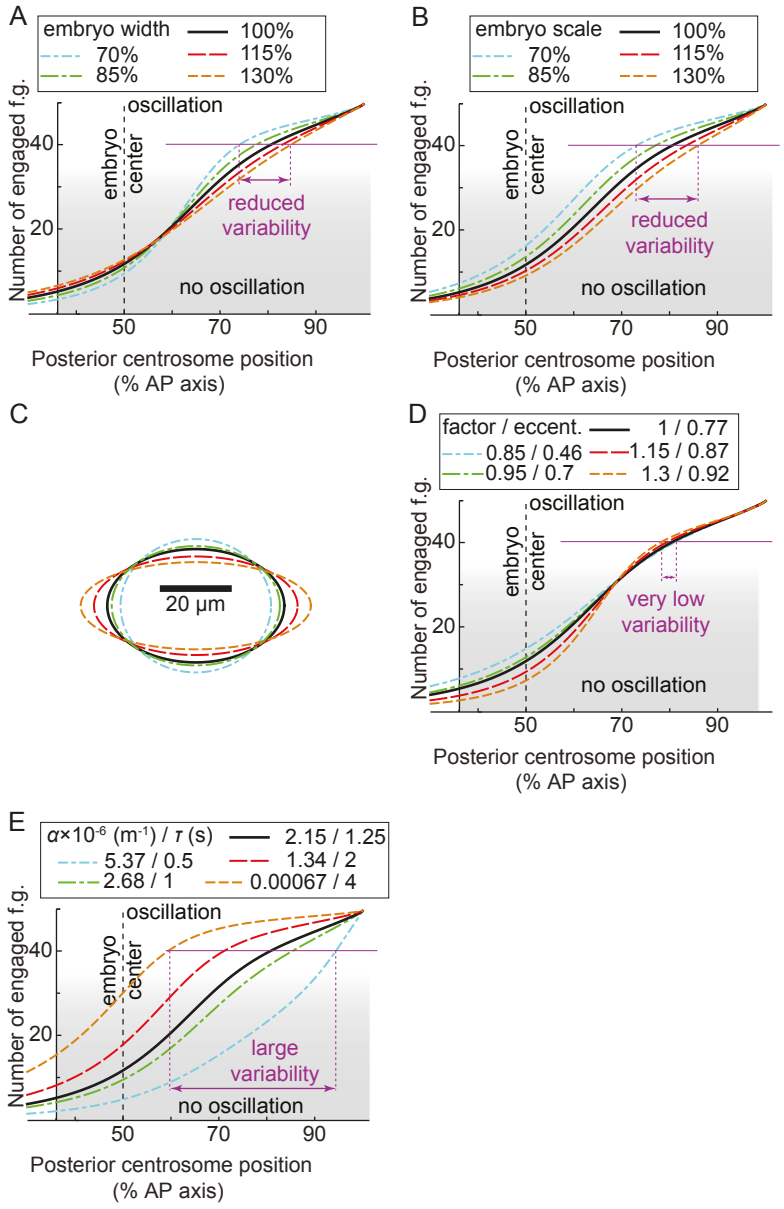
A
embryo width
100%
70%
115%
85%
130%
oscillation
embryo center
reduced variability
no oscillation
Number of engaged f.g.
Posterior centrosome position (% AP axis)
B
embryo scale
100%
70%
115%
85%
130%
oscillation
embryo center
reduced variability
no oscillation
Number of engaged f.g.
Posterior centrosome position (% AP axis)
C
20 µm
D
factor / eccent.
1 / 0.77
0.85 / 0.46
1.15 / 0.87
0.95 / 0.7
1.3 / 0.92
oscillation
embryo center
very low variability
no oscillation
Number of engaged f.g.
Posterior centrosome position (% AP axis)
E
α×10⁻⁶ (m⁻¹) / τ (s)
2.15 / 1.25
5.37 / 0.5
1.34 / 2
2.68 / 1
0.00067 / 4
oscillation
embryo center
large variability
no oscillation
Number of engaged f.g.
Posterior centrosome position (% AP axis)

Figure M4: **Oscillation onset sensitivity analysis of the expanded model.** Number of engaged force generators (f.g.), versus the posterior displacement of the centrosome along the anteroposterior (AP) axis. (A) Embryo width variations expressed as a percentage of the control. (B) Variations in embryo scale factor on length and width (keeping proportions). (C-D) Variations in the embryo shape after scaling its length by a multiplicative factor and the width by the square root of inverse of this same factor, with the ellipse eccentricity shown in panel C. Doing so, the ellipsoid of revolution modeling the embryo keeps the same volume. (E) Variations in microtubule dynamics summarized by parameter α in m ^{1} and its equivalent cortical residence time τ in second, assuming constant growth and shrinkage rates. In all cases, control values are black; green and blue are lower values; and red and orange are higher ones. The parameters used are listed in Table S5. Grey shading indicates when the number of engaged force generators was too low to permit oscillation (below threshold). Thin purple lines, of equal length in each panel, give a variability scale.

---

the trimeric complex (6, 7), and in low amount, leading to a limited number of cortical anchors (9–11). We thus asked whether a limiting areal concentration of GPR-1/2 at the cortex could alter our model predictions. In the model proposed here, we considered force generator as a reactant of binding reaction. This latter included the molecular motor dynein but also other members of the trimeric complex, as GPR-1/2. Therefore, a limited cortical areal concentration in dynein or GPR-1/2 was modeled identically as a limited areal concentration of force generator. We wrote the corresponding law of mass action in concentration:

$$\tilde{K}_a = \frac{[\text{Microtubule–force-generator}]}{[\text{Microtubule-at-cortex}]\,[\text{force-generator}]}, \tag{13}$$

with [force-generator] $= \frac{N_{\text{force-generator}}}{S_{activeRegion}}$, $\tilde{K}_a = K_a S_{activeRegion}$ and $S_{activeRegion}$ the posterior-most crescent surface (active region), whose boundary is considered at 70% of embryo length. By modeling the embryo by a prolate ellipsoid of radii 24.6 μm and twice 15.75 μm, we obtained $S_{activeRegion} \simeq 0.147\, S_{embryo} = 610\ \mu\text{m}^2$, while the whole embryo surface was $S_{embryo} \simeq 4100\ \mu\text{m}^2$.

The probability of a microtubule to hit the cortex (Eq. 3 and 5) was modified as follow:

$$\tilde{\mathcal{M}}\left(\mathcal{S}, \alpha, \theta, \phi\right) = \frac{M}{4\pi} \frac{1}{1 + \alpha\, r_{\mathcal{S}}\left(\theta, \phi\right)} \frac{1}{r_{\mathcal{S}}\left(\theta, \phi\right)^2} \tag{14}$$

We then calculated the number of engaged force generators as above (Eq. 11) and found also a positional switch (Fig. M3B compared to M3A). We concluded that this alternative modeling of force generator–microtubule attachment was compatible with the positional switch that we observed experimentally.

In contrast with the law of mass action in quantity, when the centrosome was further displaced towards the posterior after the positional switch, we did not observe any saturation in engaged force generators but a decrease (Fig. M3B). This may suggest that the centrosome position could control the oscillation die down, if diffusion of member(s) of the trimeric complex in the cortex was the limiting factor. In such a case, one would expect that die down did not intervene after a fixed delay from anaphase onset, but at a given position. This contrasted with experimental observations upon delaying anaphase onset (Table S5). Therefore, the law of mass action in quantity appeared to better model our data.

On top of this experimental argument, we estimated the lateral diffusion of the limited cortical anchors, likely GPR-1/2, and calculated a corresponding diffusion limited reaction rate equal to $k_{on}^{D} \simeq 1.2 \times 10^5$ s^{-1} after (38, 39). We considered the parameters detailed previously, a diffusion coefficient for GPR-1/2 similar to the one of PAR proteins $D = 0.2$ μm^2/s (40), and a hydrodynamic radius of 5.2 nm (41). Compared to the on-rate value proposed above (§2.2.3), i.e. $k_{on} \simeq 0.375$ s^{-1}, this suggested that lateral diffusion was not limiting. In contrast, it was proposed that in such a case, lateral diffusion may even enhance rather than limit the reaction (42). We concluded that the process was limited by reaction, not diffusion, and we considered action mass in quantity (Eq. 9a) in the remaining of this work.

2.2.7 The processivity and microtubule dynamics set two independent switches on force generators: the expanded tug-of-war model

We next asked whether a cross-talk exists between the control of the oscillation onset by the processivity, as previously reported (10), and the positional switch explained above. To do so, we let K_a varying with both the processivity $1/\overline{k_{off}}$ and the centrosome position. In the notations of the initial model, since we kept $\widehat{k_{on}}$ constant, it meant that k_{on} varied because of changes in the number of microtubule contacts in the posterior-most crescent, in turn depending on the centrosome position. We then computed the pairs $(\overline{k_{off}^{c}}, x^c)$ so that Eq. 6 was critical, i.e. $\Xi^c = \Gamma^t$ (Eq. 7), with x^c the critical position of the centrosome along the AP axis and $\overline{k_{off}^{c}}$ the critical off-rate. Because we considered the transverse axis and a single centrosome, we used $\Gamma^t = 140$ μN.s/m after (28) and obtained the diagram reproduced in (Fig. 5A) that could be seen as a stability diagram. When the embryo trajectory (the orange arrow) crosses the first critical line (collection of $(\overline{k_{off}^{c}}, x^c)$, depicted in blue) to go into the unstable region (blue area), the oscillations start and develop. Since this line is diagonal, it suggests that such an event depends upon the position of the posterior centrosome (ordinate axis) and the detachment rate (abscissa), suggesting that two control parameters contribute to making the system unstable and oscillating. Interestingly, when the embryo continues its trajectory in the phase diagram, it crosses the second critical line (depicted in green), which corresponds to the moment the system becomes stable again, and oscillations are damped out. This critical line is almost vertical indicating that this event depends mostly on the detachment rate, i.e. the inverse of processivity, consistent with the experimental observations (Table S5). Interestingly, this behavior is maintained despite modest variations in the range of processivity and centrosome position explored during the division (i.e. the precise trajectory of the embryo in this stability diagram). Note that large values of detachment rate are irrelevant as they do not allow posterior displacement of the spindle (Fig. 6G, orange curve). We concluded that two independent switches control the onset of anaphase oscillations and broadly the burst of pulling forces contributing to spindle elongation and posterior displacement.

3 Simulating posterior displacement and final spindle position

Because the cortical pulling forces involved in the anaphase spindle oscillations are also causing the posterior displacement, and because they depend on the position of the posterior centrosome, it creates a feedback loop on the posterior centrosome position. Resistance to changes of some parameters revealed by the sensitivity analysis of the oscillation onset sug-

gests that these same parameters may have a reduced impact on the final position of the centrosome. In turn, this final position is essential as it contributes to determine the position of the cytokinesis cleavage furrow, a key aspect in an asymmetric division to correctly distribute cell fate determinants (1–3).

To simulate the kinematics of posterior displacement, we considered the expanded model (§2.2) and a slowly-varying binding constant K_a due to the processivity increasing throughout mitosis (§2.2.3). We calculated the posterior pulling forces, assuming an axisymmetric distribution of force generators. The projection of the force exerted by the cortical pulling force generators implied a weakening factor because only the component parallel to the AP axis contributes to displace posteriorly the spindle. To calculate it, we made the assumption that any microtubule contacting the cortex in the active region has an equal probability to attach a force generator. Therefore, we obtained the force weakening due to the AP axis projection by writing the ratio of the forces exerted by each microtubule contacting the cortex weighted by the probability of a contact and integrated over the active region and over the number of microtubule contacts calculated using Eq. 14. This weakening ratio was then multiplied by the number of bound force generators previously obtained (Eq. 11). The weakener of the pulling force along the AP axis $\mathcal{F}$ then reads:

$$\mathcal{F}^{ante|post}\left(x, \overline{k_{off}}\right) = \frac{2\pi \int_{\theta=0}^{\theta_0^{ante|post}} p\left(\mathcal{S}, \alpha, x, \theta\right) \cos\theta \, \mathrm{d}\,\theta}{P\left(\mathcal{S}, \alpha, x\right)} \times \mathcal{N}\left(\mathcal{S}, \alpha, x, K_a^{ante|post}\right) \bar{f} \tag{15}$$

with θ_0 the polar angle of the active region boundary positioned at x_{ante}^0 and x_{post}^0, obtained assuming an ellipsoidal embryo shape. $p\left(\mathcal{S}, \alpha, x_{ante|post}, \theta\right)$ was defined at Eq. 3 and $P\left(\mathcal{S}, \alpha, x_{ante|post}\right)$ at Eq. 4. The Eq. 15 was used to calculate both anterior and posterior forces, with their respective parameters. After (8), the force asymmetry was due to an asymmetry of f.g.-MT affinity, under the control of GPR-1/2. We accounted for this asymmetric on-rate through an asymmetric attachment constant writing $K_a^{ante|post} = \beta^{ante|post} \widehat{kon} \,/\overline{k_{off}}$.

We put the above quantities into Eq 6 to finally get:

$$I^{post}\, \ddot{x}_{post} + \left(\Gamma - \Xi^{post}\right) \dot{x}_{post} + K\, x_{post} - K_{ante}\, x_{ante} = \eta + \mathcal{F}^{post}(x_{post}) - \mathcal{F}_{ante} \tag{16}$$

with η a white noise modeling the force generator stochastic attachment and detachment (10, 43). In particular, we used

$$k_{on} = \widehat{k_{on}} \left(\mathcal{M}\left(\mathcal{S}, \alpha, x_{post}\right) - \mathcal{N}\left(\mathcal{S}, \alpha, x_{post}, K_a^{post}\right)\right)$$

and also applied a weakening of anterior force to account for the uncoupling of spindle poles at anaphase onset (30, 44). With λ the weakening factor and $\overline{k_{off}^0}$ the force generator off-rate at anaphase onset, we wrote:

$$F_{ante} = \begin{cases} \mathcal{F}_{ante} & \text{if} \quad \overline{k_{off}} \geq \overline{k_{off}^0} \\ \lambda \mathcal{F}_{ante} & \text{if} \quad \overline{k_{off}} < \overline{k_{off}^0} \end{cases} \tag{17a}$$

(17b)

Similarly, the centering force (16, 28) was also weakened:

$$K_{ante} = \begin{cases} K & \text{if} \quad \overline{k_{off}} \geq \overline{k^0_{off}} \\ \lambda K & \text{if} \quad \overline{k_{off}} < \overline{k^0_{off}} \end{cases} \tag{18a}$$

$$\tag{18b}$$

We solved this system numerically using trapezoidal rule and backward differentiation formula of order 2 (TR-BDF2 algorithm) (21). Since we linearized the equations and kept the anterior centrosome at a fixed position, we could explore only reasonable parameter variations when performing the final position parameter sensitivity analysis (Fig. 6D-H, M5). As a sanity check, we observed that modest variations in the force generator on-rate, thought to translate polarity cues (8), modulated the final spindle position (Fig. 6E) as expected from experiments (5, 26). To ensure that our simulation correctly converged to the true final position, we varied the initial spindle position and observed no significant change in its final position (Fig. M5C).

4 Conclusion

We previously proposed that the final centrosome position was dictated both by the centering force stiffness and by the imbalance in pulling force generation, i.e. mainly the active force generator number in active region and their processivity (10). In contrast, in the full-expanded model, when the posterior centrosome enters into the active region, more microtubules are oriented along the transverse axis than parallel to the AP axis because of the isotropic distribution of the microtubules around the centrosome. Then, this limits the pulling forces on the posterior centrosome (Fig. S3D). As a consequence, the boundary of the active region sets the final position of the posterior centrosome as seen experimentally ((13) and this study). In contrast, the force generator quantity and dynamics become less important and the final spindle position even shows some resistance to changes in these two parameters (Fig. 6E-G).

We noticed that when the active region boundary was located at 80% of embryo length or more posteriorly, and the spindle was close to the cell center, the number of microtubules reaching this region was so reduced that it prevented a normal posterior displacement of the spindle. Together with the observation that when the region extended more anteriorly the final spindle position was anteriorly shifted (Fig. 6ABD), it appeared that a boundary at 70% was a value quite optimal to maximize the posterior displacement. Because this posterior displacement is a key to asymmetric division, it would be interesting (but out of the scope of this work) to see whether a maximal posterior displacement is an evolutive advantage, which would then cause a pressure on the active region boundary.

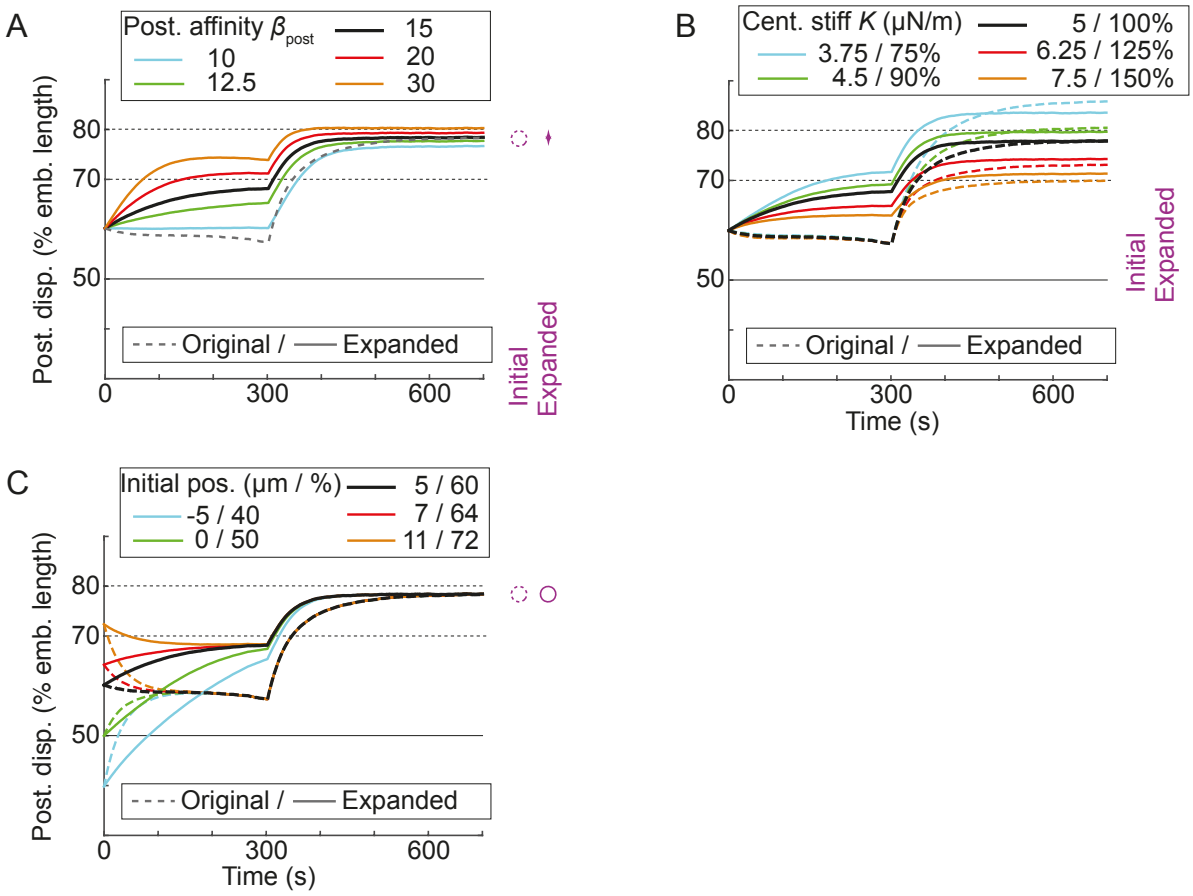

Figure M5: **Final spindle position sensitivity analysis of the full-expanded model.** Stochastic simulations of the posterior centrosome displacement. Dashed lines represent the results of the initial model (10), while solid lines correspond to the full-expanded one. Posterior displacement of the posterior centrosome averaged over 25 simulation runs with respectively varied: (A) the posterior affinity of the f.g. for microtubule (on-rate) β, whose asymmetry may encode the polarity (8); (B) the centering spring used to model centering forces (16); and (C) the initial position of the posterior centrosome. When it does not depend on the parameter considered, the original model is shown by a dashed grey line. In all cases, the control values are black; lower values are blue and green; and the higher values are red and orange. The dispersions of the final values for each case are represented by purple arrows, and a larger span in the plot reveals a lack of robustness to parameter variations. A circle is used when the parameter has no effect on the final value. The parameters used are listed in Table S5.

Supporting References

1. White, E. A., and M. Glotzer. 2012. Centralspindlin: At the heart of cytokinesis. Cytoskeleton (Hoboken) 69:882-892.
2. Rappaport, R. 1971. Cytokinesis in animal cells. Int Rev Cytol 31:169-213.
3. Knoblich, J. A. 2010. Asymmetric cell division: recent developments and their implications for tumour biology. Nat Rev Mol Cell Biol 11:849-860.
4. Nguyen-Ngoc, T., K. Afshar, and P. Gonczy. 2007. Coupling of cortical dynein and G alpha proteins mediates spindle positioning in *Caenorhabditis elegans*. Nat Cell Biol 9:1294-1302.
5. Colombo, K., S. W. Grill, R. J. Kimple, F. S. Willard, D. P. Siderovski, and P. Gonczy. 2003. Translation of polarity cues into asymmetric spindle positioning in *Caenorhabditis elegans* embryos. Science 300:1957-1961.
6. Park, D. H., and L. S. Rose. 2008. Dynamic localization of LIN-5 and GPR-1/2 to cortical force generation domains during spindle positioning. Dev Biol 315:42-54.
7. Riche, S., M. Zouak, F. Argoul, A. Arneodo, J. Pecreaux, and M. Delattre. 2013. Evolutionary comparisons reveal a positional switch for spindle pole oscillations in *Caenorhabditis embryos*. J Cell Biol 201:653-662.
8. Rodriguez Garcia, R., L. Chesneau, S. Pastezeur, J. Roul, M. Tramier, and J. Pecreaux. 2017. Dynein dynamics at the microtubule plus-ends and cortex during division in the *C. elegans* zygote. bioRxiv:118604.
9. Grill, S. W., J. Howard, E. Schaffer, E. H. Stelzer, and A. A. Hyman. 2003. The distribution of active force generators controls mitotic spindle position. Science 301:518-521.
10. Pecreaux, J., J. C. Roper, K. Kruse, F. Julicher, A. A. Hyman, S. W. Grill, and J. Howard. 2006. Spindle oscillations during asymmetric cell division require a threshold number of active cortical force generators. Curr Biol 16:2111-2122.
11. Grill, S. W., K. Kruse, and F. Julicher. 2005. Theory of mitotic spindle oscillations. Phys Rev Lett 94:108104.
12. Kozlowski, C., M. Srayko, and F. Nedelec. 2007. Cortical microtubule contacts position the spindle in *C. elegans* embryos. Cell 129:499-510.
13. Krueger, L. E., J. C. Wu, M. F. Tsou, and L. S. Rose. 2010. LET-99 inhibits lateral posterior pulling forces during asymmetric spindle elongation in *C. elegans* embryos. J Cell Biol 189:481-495.
14. Howard, J. 2006. Elastic and damping forces generated by confined arrays of dynamic microtubules. Phys Biol 3:54-66.
15. Srayko, M., A. Kaya, J. Stamford, and A. A. Hyman. 2005. Identification and characterization of factors required for microtubule growth and nucleation in the early *C. elegans* embryo. Dev Cell 9:223-236.
16. Pecreaux, J., S. Redemann, Z. Alayan, B. Mercat, S. Pastezeur, C. Garzon-Coral, A. A. Hyman, and J. Howard. 2016. The mitotic spindle in the one-cell *C. elegans* embryo is positioned with high precision and stability. Biophys J 111:1773-1784.
17. Roul, J., J. Pecreaux, and M. Tramier. 2015. Method for controlling a plurality of functional modules including a multi-wavelength imaging device, and corresponding control system. E. P. Office WO2015144650 A1.
18. Kalman, R. E. 1960. A new approach to linear filtering and prediction problems. Journal of Basic Engineering 82:35-45.

19. Jaqaman, K., D. Loerke, M. Mettlen, H. Kuwata, S. Grinstein, S. L. Schmid, and G. Danuser. 2008. Robust single-particle tracking in live-cell time-lapse sequences. Nat Methods 5:695-702.
20. Pecreaux, J., C. Zimmer, and J. C. Olivo-Marin. 2006. Biophysical active contours for cell tracking I: Tension and bending. In Ieee International Conference on Image Processing (Icip), October 8-11 2006, Atlanta, GA, USA. 1949-1952.
21. Hosea, M. E., and L. F. Shampine. 1996. Analysis and implementation of TR-BDF2. Applied Numerical Mathematics 20:21-37.
22. O'Toole, E. T., K. L. McDonald, J. Mantler, J. R. McIntosh, A. A. Hyman, and T. Muller-Reichert. 2003. Morphologically distinct microtubule ends in the mitotic centrosome of *Caenorhabditis elegans*. J Cell Biol 163:451-456.
23. Labbe, J. C., E. K. McCarthy, and B. Goldstein. 2004. The forces that position a mitotic spindle asymmetrically are tethered until after the time of spindle assembly. J Cell Biol 167:245-256.
24. Koonce, M. P., and I. Tikhonenko. 2012. Dynein Motor Mechanisms. In Dyneins : structure, biology and disease. S. M. King, editor. Academic Press, Amsterdam ; Boston. xv, 639 p.
25. Farhadifar, R., J. M. Ponciano, E. C. Andersen, D. J. Needleman, and C. F. Baer. 2016. Mutation is a sufficient and robust predictor of genetic variation for mitotic spindle traits in *Caenorhabditis elegans*. Genetics 203:1859-1870.
26. Grill, S. W., P. Gonczy, E. H. Stelzer, and A. A. Hyman. 2001. Polarity controls forces governing asymmetric spindle positioning in the *Caenorhabditis elegans* embryo. Nature 409:630-633.
27. Kimura, A., and S. Onami. 2007. Local cortical pulling-force repression switches centrosomal centration and posterior displacement in *C. elegans*. J Cell Biol 179:1347-1354.
28. Garzon-Coral, C., H. A. Fantana, and J. Howard. 2016. A force-generating machinery maintains the spindle at the cell center during mitosis. Science 352:1124-1127.
29. Redemann, S., J. Baumgart, N. Lindow, M. Shelley, E. Nazockdast, A. Kratz, S. Prohaska, J. Brugues, S. Furthauer, and T. Muller-Reichert. 2017. C. elegans chromosomes connect to centrosomes by anchoring into the spindle network. Nat Commun 8:15288.
30. Maton, G., F. Edwards, B. Lacroix, M. Stefanutti, K. Laband, T. Lieury, T. Kim, J. Espeut, J. C. Canman, and J. Dumont. 2015. Kinetochore components are required for central spindle assembly. Nat Cell Biol 17:697-705.
31. Gierke, S., P. Kumar, and T. Wittmann. 2010. Analysis of microtubule polymerization dynamics in live cells. Methods in cell biology 97:15-33.
32. Laan, L., N. Pavin, J. Husson, G. Romet-Lemonne, M. van Duijn, M. P. Lopez, R. D. Vale, F. Julicher, S. L. Reck-Peterson, and M. Dogterom. 2012. Cortical dynein controls microtubule dynamics to generate pulling forces that position microtubule asters. Cell 148:502-514.
33. Olson, S. K., G. Greenan, A. Desai, T. Muller-Reichert, and K. Oegema. 2012. Hierarchical assembly of the eggshell and permeability barrier in *C. elegans*. J Cell Biol 198:731-748.
34. Costantino, S., J. W. Comeau, D. L. Kolin, and P. W. Wiseman. 2005. Accuracy and dynamic range of spatial image correlation and cross-correlation spectroscopy. Biophys J 89:1251-1260.
35. Ahringer, J. 2003. Control of cell polarity and mitotic spindle positioning in animal cells. Current Opinion in Cell Biology 15:73-81.

36. Edwards, J. 1892. An elementary treatise on the differential calculus, with applications and numerous examples. Macmillan, London, New York,.
37. Farhadifar, R., C. F. Baer, A. C. Valfort, E. C. Andersen, T. Muller-Reichert, M. Delattre, and D. J. Needleman. 2015. Scaling, selection, and evolutionary dynamics of the mitotic spindle. Curr Biol 25:732-740.
38. Freeman, D. L., and D. J. D. 1983. The influence of diffusion on surface reaction kinetics. The Journal of Chemical Physics 78:6002.
39. Freeman, D. L., and J. D. Doll. 1983. Langevin analysis of the diffusion model for surface chemical reactions. The Journal of Chemical Physics 79:2343.
40. Goehring, N. W., C. Hoege, S. W. Grill, and A. A. Hyman. 2011. PAR proteins diffuse freely across the anterior-posterior boundary in polarized *C. elegans* embryos. J Cell Biol 193:583-594.
41. Erickson, H. P. 2009. Size and shape of protein molecules at the nanometer level determined by sedimentation, gel filtration, and electron microscopy. Biol Proced Online 11:32-51.
42. Adam, G., and M. Delbruck. 1968. Reduction of dimensionality in biological diffusion processes. In Structural Chemistry and Molecular Biology. A. Rich, N. R. Davidson, and L. Pauling, editors. W. H. Freeman, San Francisco. 198-215.
43. Nadrowski, B., P. Martin, and F. Julicher. 2004. Active hair-bundle motility harnesses noise to operate near an optimum of mechanosensitivity. Proc Natl Acad Sci U S A 101:12195-12200.
44. Mercat, B., X. Pinson, J. Fouchard, H. Mary, S. Pastezeur, Z. Alayan, Y. Gachet, S. Tournier, H. Bouvrais, and J. Pecreaux. 2016. Spindle micro-fluctuations of length reveal its dynamics over cell division. Biophysical Society meeting, Los Angeles (CA), USA. In Biophys J 110:622a.